Thermoreflectance imaging of electromigration evolution in asymmetric aluminum constrictions

Hao Tian, Woojin Ahn, Kerry Maize, Mengwei Si, Peide Ye, Muhammad Ashraful Alam, Ali Shakouri, and Peter Bermel

---

Thermoreflectance imaging of electromigration evolution in asymmetric aluminum constrictions

Hao Tian,[a] Woojin Ahn, Kerry Maize, Mengwei Si, Peide Ye, Muhammad Ashraful Alam, Ali Shakouri, and Peter Bermel
Birck Nanotechnology Center, Purdue University, West Lafayette, Indiana 47907, USA

Electromigration (EM) is a phenomenon whereby the flow of current in metal wires moves the underlying atoms, potentially inducing electronic interconnect failures. The continued decrease in commercial lithographically defined feature sizes means that EM presents an increasing risk to the reliability of modern electronics. To mitigate these risks, it is important to look for novel mechanisms to extend lifetime without forfeiting miniaturization. Typically, only the overall increase in the interconnect resistance and failure voltage are characterized. However, if the current flows non-uniformly, spatially resolving the resulting hot spots during electromigration aging experiments may provide better insights into the fundamental mechanisms of this process. In this study, we focus on aluminum interconnects containing asymmetric reservoir and void pairs with contact pads on each end. Such reservoirs are potential candidates for self-healing. Thermoreflectance imaging was used to detect hot spots in electrical interconnects at risk of failure as the voltage was gradually increased. It reveals differential heating with increasing voltage for each polarity. We find that while current flow going from a constriction to a reservoir causes a break at the void, the identical structure with the opposite polarity can sustain higher current ($J = 21 \times 10^6$ A/cm^2) and more localized joule heating and yet is more stable. Ultimately, a break takes place at the contact pad where the current flows from narrow interconnect to larger pads. In summary, thermoreflectance imaging with submicron spatial resolution provides valuable information about localized electromigration evolution and the potential role of reservoirs to create more robust interconnects. *Published by AIP Publishing.* https://doi.org/10.1063/1.5005938

I. INTRODUCTION

Electromigration (EM) is a phenomenon whereby strong electric currents move the atoms in a wire, potentially inducing electronic interconnect failures.[1–3] As electrons move from the cathode to the anode, they collide with metal ions and transfer momentum to individual atoms, moving them in the direction of the electron wind. This electron-associated force can be so large under high current density that it will overcome the confinement of the crystalline lattice and the electric field in the metal wire.[2,4] Gradually, the atoms in the interconnect wires are displaced into hillocks and voids at grain boundaries,[5] which may cause severe problems in circuits, such as the fracturing of interconnects via large voids and the formation of short circuits from hillocks. Previous work has identified the basic phenomenology of EM failures and mitigation strategies.[6] For example, researchers have utilized physical designs and optimized circuit designs to reduce the current density,[7–9] such as structures designed to avoid current crowding and wiring topology optimization. Some researchers have designed optimal architectures to mitigate electromigration.[10–12] For instance, when the wire width is narrow enough, it forms bamboo-like grain boundary structures which protect the atoms from moving with the electron wind.[4,6,13] For short interconnects below the so-called Blech length (typically 10–100 μm), a mechanical stress gradient is established along the line, helping the atoms move against the electron wind.[3,4,14,15] Copper doping in the Al film has also been found to reduce electromigration risk,[16,17] which may retard atom transport along the grain boundaries.[16] In addition, the reservoir effect, which elongates the lifetime of an interconnect by placing extra material source near potential voids, has been studied for electromigration mitigation.[18,19]

Although EM is now much better understood, the continuing decrease in commercial lithographically defined feature sizes has generally increased the current density, thus raising the risk of more frequent EM failures.[20] To mitigate this risk, it is important to develop characterization methods that can reveal localized current flow non-uniformities and hot spots, as well as novel mechanisms that can extend the lifetime without forfeiting miniaturization. Recently, the observation of electromigration of Au nanowires in real time has been implemented by Taychatanapat *et al.*[21] using scanning electron microscopy. Furthermore, the nanoscale temperature distribution of Au nanowires during electromigration has been studied by Jeong *et al.*,[22] showing asymmetric hotspot evolution and microvoid formation. In this work, asymmetric constrictions and a potential self-healing structure using the reservoir effect in a constant-volume line are studied. The latter seeks to continually refill voids to improve the reliability of interconnects. Specifically, a material reservoir is placed near an intentionally added void on the metal wire as shown in Fig. 1(a). The material we mainly

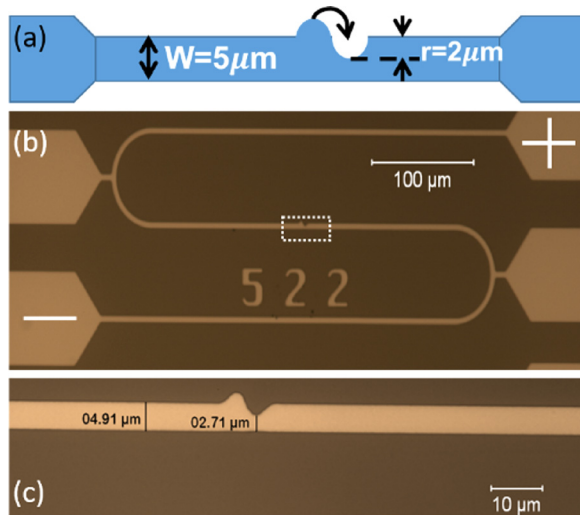a)Author to whom correspondence should be addressed: tian90@purdue.edu

FIG. 1. (a) Schematic of the asymmetric interconnect test structure, consisting of a void and reservoir. The test line width is 5 μm, and the radius of the void and reservoir is 2 μm. (b) Fabricated Al interconnect imaged via an optical microscope. The definition of forward polarity is shown. (c) Magnified view of the dashed white box from (b), showing the void and reservoir.

focus on is aluminum, which is commonly used in integrated circuits and known to be susceptible to electromigration.[23–25] Thermoreflectance imaging (TRI)[26,27] is used to observe the temperature spatial distribution and detect hot spots as the stress level is increased. This provides a snapshot of the current density profile in the device and the weak points that eventually lead to breakdown. Compared with the scanning thermal microscopy used by Jeong *et al.*,[22] which scans point by point, TRI possesses the advantages of being faster, thus providing larger regions for detailed observation. Due to the asymmetry of the designed devices, we find completely different electromigration failure modes for each bias polarity, showing significantly different lifetimes. In addition, the formation of hot spots is found to play an important role in both the failure modes, which is related to electromigration-induced structure degradation.

The methodology of this study is provided in Sec. II, which includes fabrication of the test devices using photolithography and lift-off processes and the thermoreflectance imaging system used to characterize electromigration. The results of forward polarity testing are then presented and analyzed in Sec. III, showing hotspot formation both near the void and contact pad and the device breakdown at the cathode contact pad. The case of reverse polarity is also described for comparison, which is characterized by a shorter lifetime, with failures occurring at the interconnect voids. In Sec. IV, the reasons for asymmetry results are discussed to help interpret the experimental results and provide guidance for future electromigration investigation. Finally, the manuscript concludes with Sec. V, which summarizes the main findings of this study.

II. METHODS

The proposed asymmetric interconnect test structure is illustrated in Fig. 1(a), which consists of an aluminum (Al)

test line with a void and reservoir pair that has the same average volume per unit length as the ordinary interconnect line to which it is connected. Here, the interconnect line width is 5 μm, and the radius of the void and reservoir is 2 μm. It is designed with a length of 1250 μm to provide reasonable resistance in measurements. The device is fabricated on silicon dioxide (200 nm thickness), which is grown by thermal dry oxidation on top of a standard Si wafer and serves as an insulation layer. The fabrication procedure follows standard photolithography and lift-off processes. A positive photoresist (AZ 1518) is first applied to the wafer using a G3 Wafer Spinner, and the pattern is then transferred from the mask to photoresist by exposing the wafer under UV light in the mask aligner (Suss MA6 Mask Aligner, exposure of 13 s), followed by development in the developer (AZ 340: ultra-pure water ratio of 1:4) for 10–12 s. 110 nm Al is deposited on the wafer using e-beam evaporation (CHA e-beam evaporator) with a deposition rate of 3 Å/s. Finally, the sample is soaked in acetone until all the Al deposited on the photoresist is peeled off. During the soaking, the beaker containing the wafer is placed in an ultrasonic water bath for 5–10 s, which helps to lift-off the unwanted metal.

Figures 1(b) and 1(c) show the resulting optical microscopy images of the fabricated device. Since the total length of the test line is relatively long, the actual device is rotated as a serpentine line for better thermoreflectance imaging and observation. Two different bias polarities are applied to the device in this study, while the forward polarity is defined in Fig. 1(b).

The principle of thermoreflectance imaging is illustrated in Fig. 2(a).[28,29] Electrical square wave pulses (pulse width = 1 ms, duty cycle = 10%, and modulation frequency = 100 Hz) are applied to the test line, inducing Joule heating in the metal and a corresponding change in material reflectance.
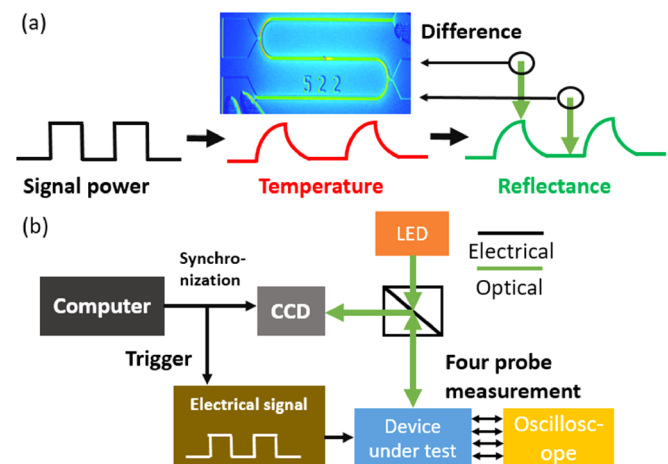

FIG. 2. (a) Schematic of the principle of thermoreflectance imaging. Pulses are applied to the device, while the reflectance of light is measured, which is related to the temperature. The differential image between high and low reflectance shows changes and distribution of the temperature. The inset shows the typical temperature distribution of the whole device. (b) Schematic of the thermoreflectance imaging system. An LED light is used to illuminate the device, and a CCD is used to detect the reflected light from the device. A computer synchronizes the triggering of the electrical signal and detection of reflection. The current and voltage of the devices are monitored by the oscilloscope using a four probe measurement.
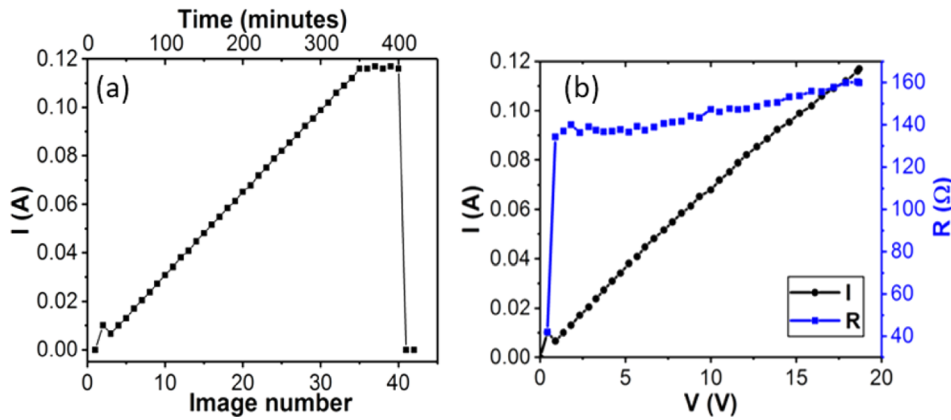
FIG. 3. (a) Change in current with the image number and time (top horizontal axis). Each image accounts for 10 min. The output current from the current source reaches the maximum value after image 35. (b) Change in current (black line) and resistance (blue line) with increasing voltage, showing the gradually increasing resistance of the test line.

Separate experimental calibration of the aluminum temperature coefficient of thermal reflectance (CTR) at the probe wavelength of 780 nm yields a CTR value of 1.4×10^{-4} per °C. The spatial distribution of temperature is obtained by taking the difference between the images acquired during the time windows in the excitation waveform corresponding to the device active (hot) and passive (equilibrium) states. Note that the temperature measured is the temperature change (ΔT) relative to room temperature (approximately 25 °C). Figure 2(b) shows the schematic of the Microsanj Inc. NT 210 thermoreflectance imaging system used, which includes signal generation, probe illumination, CCD detection, and electrical measurement systems. The sample wafer is placed on a copper heat sink at the focal plane of a conventional reflectance microscope. The device is electrically probed on the wafer using a four-probe configuration. Pulsed probe light-emitting diode (LED) illumination centered at 780 nm is coupled to the microscope and illuminates the sample over the full field of view. The sample reflected intensity is recorded using a 12-bit Dalsa CCD coupled to the microscope. The device pulse waveform is generated by a function generator and amplified by a current source. The device current and voltage during thermoreflectance excitation are monitored by an oscilloscope using a four probe measurement. A Melles Griot 313 piezo actuator and a custom Microsanj image registration algorithm automatically correct for defocusing or image shift from thermal expansion of the microscope during image averaging. All these systems are synchronized by hardware triggers and processed by Microsanj software. Since the device material reflectance changes only slightly for the applied modulation, each image is averaged over 10 min for a higher signal-to-noise ratio.

III. RESULTS AND ANALYSIS

A. Forward polarity

The sample is first tested under forward polarity (i.e., a forward voltage bias), as shown in Fig. 3(a). While two separate trials were performed under these conditions, both results were very similar, and so, only the second trial is presented for simplicity. During this test, the output current from the current source increases by a constant amount every ten minutes, reaching a maximum output value around 0.12 A (corresponding to a current density $J = 21 \times 10^6$ A/cm²), which is kept constant after image 35. Figure 3(b) shows that

the current and resistance of the device increase linearly with voltage. The low initial resistance and current spike are mainly caused by the limited resolution of the oscilloscope.

The change in temperature distribution around the void and contact pad from images 36 to 42 is illustrated in Fig. 4(a). The high current density near the void gives rise to Joule heating and eventually a high temperature region that grows with increasing bias. It should be noted that the device breakdown occurs during image 40, and the relatively high temperature of image 41 corresponds to slow cooling of the whole device. As for the pad, an observable hot spot forms right near the neck of the contact pad, which leads to the final failure of the test line. The device is then imaged after failure in Figs. 4(b) and 4(c). Microvoids form around the void and to its right, mainly due to electromigration. Interestingly, microvoids form upstream from the electron
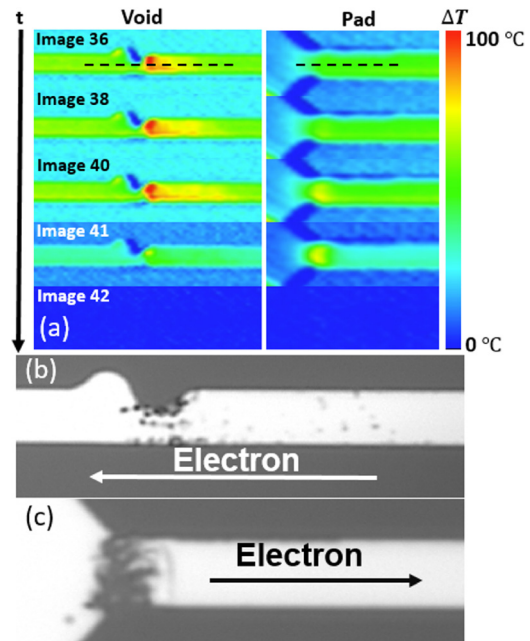

FIG. 4. (a) Change in temperature distribution around the void (left) and contact pad (right) right before device breakdown under forward polarity. The current density J of these images is all 21×10^6 A/cm². A hot spot forms near the pad, leading to failure of the device. SEM micrographs near (b) the void and (c) the pad after the device breakdown are shown. Microvoids are formed near the void due to electromigration. The failure of the device occurs at the contact pad, as is evident from the clear disconnect between the test line and the pad.
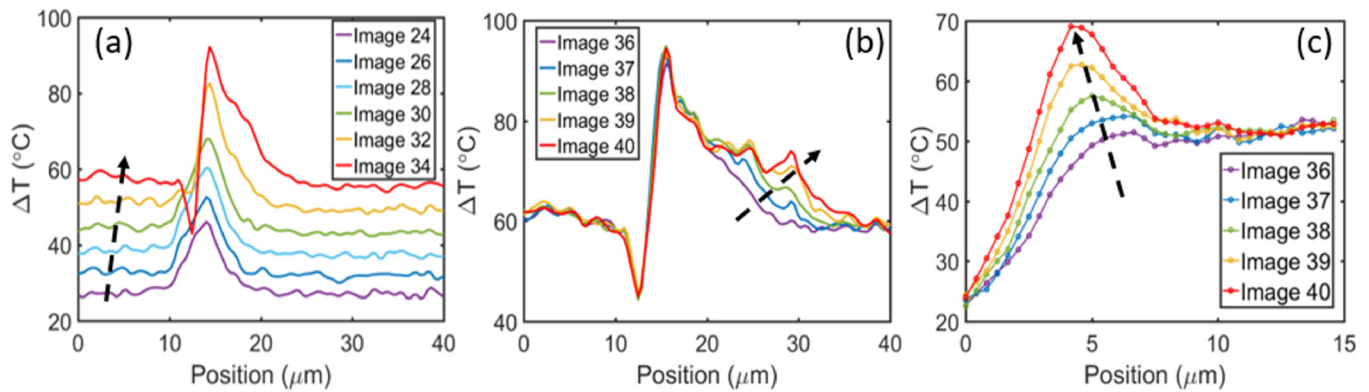
FIG. 5. Change in temperature distribution along the black dashed line near [(a) and (b)] the void and (c) pad in Fig. 4(a). The temperature dip near the void from images 34 to 40 is due to the electromigration-induced microvoids. (c) The formation of the hot spot near the contact pad. The black dashed arrow in each figure shows the trend of the increasing image number, which also corresponds to increasing time and voltage.

wind, in the high temperature region of Fig. 4(a). Although some defects appear near the void, the device in fact fails at the pad [Fig. 4(c)], caused by a disconnection between the contact pad and wire line. Since defects are formed at both locations, it is also possible that additional trials could yield failures at the void in some cases.

The temperature distribution along the black dashed line near the void and pad of Fig. 4(a) is plotted in Fig. 5. From the temperature distribution for the void [Fig. 5(a)], as current density increases linearly from 14×10^6 to 20×10^6 A/cm^2, the temperature on the line also increases linearly. It increases most rapidly near the void, caused by the higher local current density. Interestingly, an apparent temperature dip is observed under the void for image 34 (red line), which can be explained by the formation of an initial microvoid. Since the CTR of Al is positive (i.e., higher temperature means higher reflection) and the temperature and reflectance of the substrate (covered by SiO$_2$) are much lower than those of the device (made from Al), the measured averaged temperature over the microvoid will be smaller, corresponding to the area of the dip. This hypothesis could be fully verified by calibrating the thermoreflectance coefficient in this region, which is a possible subject for future studies. As the current plateaus [Fig. 5(b)], the hot spot near the microvoid grows, which may be caused by electromigration. Another hot spot gradually emerges near the neck of the pad, with peak temperatures approaching 70 °C, well above the temperature on the line 10 μm from the hot spot, which stays around 50 °C. Since the temperature on the pad (0 μm along

the line) is relatively low (25 °C), a large temperature gradient forms between the pad neck and the wire line.

Figure 6(a) shows the evolution of temperature as a function of time in different areas near the void, as defined in the inset. Boxes 1 and 2, which are close to the void, initially have similar high temperatures. However, as the applied bias increases, the temperature of box 1 stops increasing and then gradually drops, which corresponds to the apparent temperature dip in Figs. 5(a) and 5(b). On the other hand, the temperature box 2 keeps increasing, reaching its maximum value after the current reaches a plateau. The other temperature boxes show similar but weaker trends. Box 5, which is far from the void, serves as a reference to indicate the overall temperature of the test line. It increases gradually and remains constant after the current saturates. By comparison, box 3, which is close to the hot spot, increases faster than box 5, up to the current plateau. Box 4 behaves similarly but keeps increasing even after the current plateaus, which is consistent with the diffusion of heat from the hot spot in Fig. 4(a).

A similar analysis is applied to the pad, as shown in Fig. 6(b). Box 3 works as a reference and shows the temperature changes on the line far from the hot spot. The temperatures of boxes 1 and 2 are initially lower than that of box 3 since they are closer to the pad, which has lower Joule heating and so is initially cooler. However, box 1 keeps increasing until the device breakdown, showing the exponential growth of the hot spot near the neck of the contact pad. As a result, the contact pad fails before the structure with the artificially
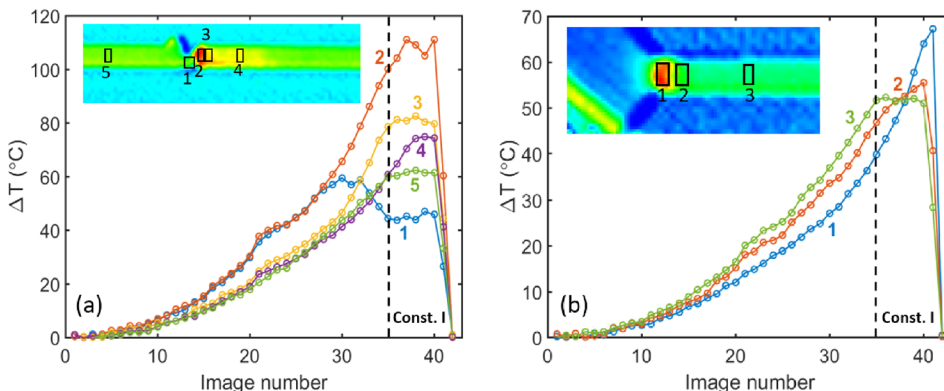

FIG. 6. Evolution of average temperature at different areas near (a) the void and (b) pad. The temperature is averaged in black boxes as indicated and labeled in the inset (image 40) of each figure. The current and voltage increase as the image number increases, while the current stays constant (J = 21 $\times 10^6$ A/cm^2) after the black dashed line, which causes most temperatures in the device to plateau, except box 1 near the pad.
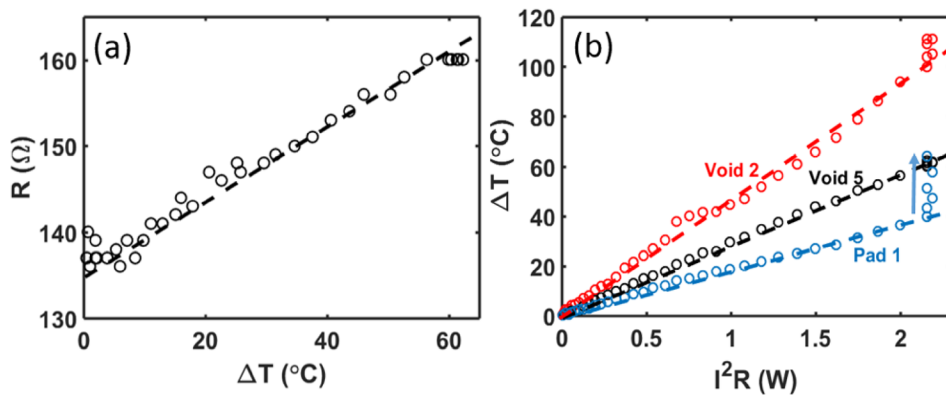
FIG. 7. (a) Resistance as a function of the temperature of box 5, which represents the average temperature of the whole device. The measured resistance saturates with the limits of the current source. (b) Dependence of temperature on Joule heating power for box 2 (red circle) and box 5 (black circle) near the void and for box 1 (blue circle) of the pad in Fig. 6. The blue arrow captures a temperature rise at the hot spot near the pad that goes beyond Joule heating. The corresponding dashed lines in the figures are added only as the guide to the eye.

introduced void. This behavior may relate to microvoid formation from electromigration, which causes local structure and current density changes. The ultimate failure at the contact pad implies that the reservoir may help preserve the functionality of the central artificial void in this polarity. Because the contact pad fails before the void in these trials, the precise improvement at the level of reliability of the artificial void cannot be fully quantified. Moreover, a high temperature gradient between the pad and wire line would accelerate the degradation and void formation near the cathode contact pad.[30] It is interesting to note that the hot spot with the highest absolute temperature along the interconnect is not the one that fails first. Thus, the local structure, the current density, and the temperature gradient should be considered in a manner that goes beyond Black's equation.[1]

The resistivity of Al increases linearly with temperature,[31] as can be seen in Fig. 7(a), based on box 5 temperature data in Fig. 6(a). Since the interconnect is relatively long, the influence of electromigration-induced local resistance changes is not evident at first. To further investigate the main cause of the temperature rise, the relation between temperature and Joule heating is illustrated in Fig. 7(b). Three different areas are studied: the hot spots near the void (void 2) and the pad (pad 1), as well as the area on the line far from these hot spots (void 5). All temperatures increase linearly with Joule power at different rates, which are related to local conditions such as current density and thermal conduction. However, while the average interconnect line reaches a temperature plateau after current saturation (void 5), the temperature of the two hot spots increases beyond general Joule power of the whole device. This is highly

related to the electromigration-induced local structural deformation, which in turn affects the current distribution and accelerates the hotspot growth.

B. Reverse polarity

Next, the device is tested at reverse polarity with other conditions unchanged. In contrast with the case of forward polarity, the breakdown occurs here before the current saturates [Fig. 8(a)], and the device fails near the artificial void instead of the contact pad. While two separate trials were performed, both results were very similar, and so, only the second trial is presented for simplicity. As shown in Fig. 8(b), the resistance also increases gradually, as Joule heating raises the device temperature. This also creates a hot spot near the void that grows rapidly as current density increases [Fig. 9(a)]. At the beginning of image 32, the device breaks immediately when the current density is increased to $19 \times 10^6 \, A/cm^2$. Then, it cools down, which pulls down the average temperature of image 32. However, the hot spot near the void can still be seen clearly in image 32. Figure 9(b) shows a micrograph of the void region after failure, which shows the microvoids induced by electromigration. The slit-like void shape may be due to the electromigration-induced diffusion along the void surface[32,33] and is influenced by the orientation of crystallographic surface planes and grain boundaries in the metal.[34–36]

The cross-sectional temperature distribution along the black dashed line in Fig. 9(a) is plotted in Fig. 10(a), showing increasing temperature with time. The temperature of the hot spot is greater than the surrounding line by more than $25\,°C$, and increases more quickly with applied voltage.
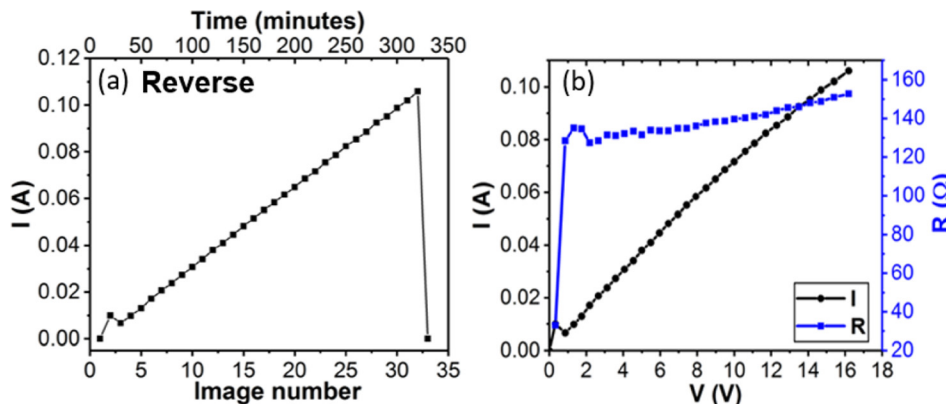

FIG. 8. (a) Change in current with the image number and time (top horizontal axis). Each image accounts for 10 min. (b) Change in current (black line) and resistance (blue line) with increasing voltage. In this test, the current increases linearly without reaching the maximum output of the current source.
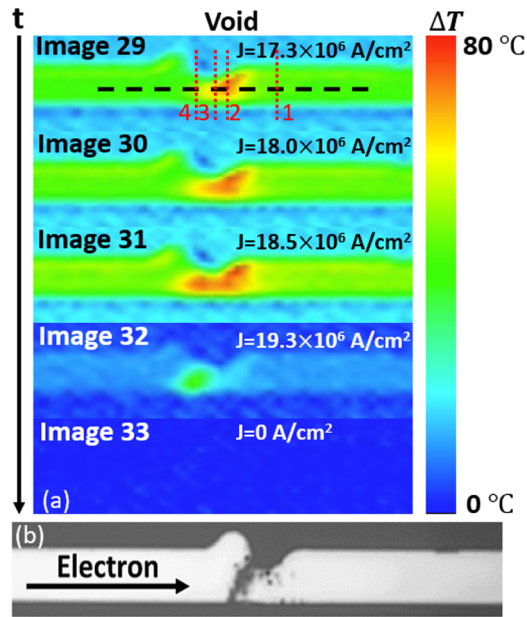
FIG. 9. (a) Change in temperature distribution around the void right before the device breakdown under reverse polarity. The hot spot formed near the void leads to the failure of the device. (b) SEM micrograph near the void after the device breakdown. Microvoids are formed near the void due to electromigration.
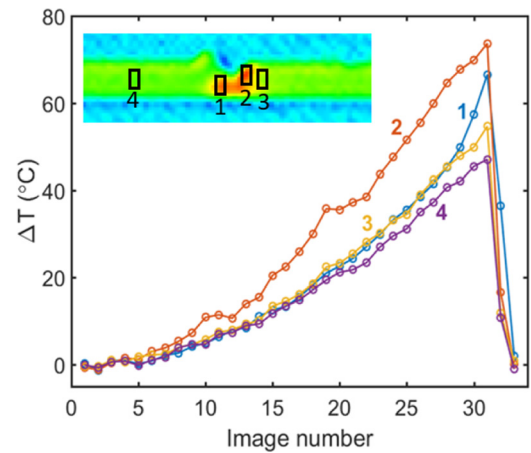

FIG. 11. Evolution of the average temperature of different areas near the void. The temperature is averaged in black boxes as indicated and labeled in the inset (image 31). Box 4 is added as an indication of the overall temperature of the device for reference. The increase in the image number corresponds to the stress level increase applied to the device.

Interestingly, for image 31, an apparent temperature dip under the void emerges, presumably because of microvoid formation, which was also seen in the case of forward polarity (Fig. 5). Figure 10(b) shows the temperature distribution perpendicular to the test line, along red dashed lines in Fig. 9(a). Cross-section 1 in the upper left serves as a reference for temperature increases far from the hot spot. Cross-section 2 in the upper right shows the highest temperature, which is in the middle of the initial hot spot. Although cross-section 3 on the lower left is in the narrowest region of the void, it is slightly cooler than the hot spot. Intriguingly, the device does not break at the hottest area but rather at a secondary hot spot at cross-section 4 (in the lower right), which may match the microvoid formation. From its temperature changes, we can see that there is a large temperature jump at image 31, which may weaken the strength of the interconnection. On the other hand, the accelerated temperature increase is highly related to the local structure deformation (e.g., microvoids) caused by electromigration, and the current density increases in the narrow region around microvoids.

The evolution of temperature around the void is also analyzed as a function of time, as shown in Fig. 11. Four different areas, labeled in the inset, are plotted here. As the applied power increases, the temperatures of all regions rise with Joule heating. As expected, box 4, which is far from the void, has the lowest temperature and shows the overall temperature changes of the whole device. Box 2 illustrates the growth of the hot spot, which is heated the most by the local current density distribution. Boxes 1 and 3 show temperatures similar to box 4 initially but deviate from its trend over time. Box 3 shows a slightly higher temperature since it is closer to the hot spot, while box 1 exhibits more dramatic increases after image 29, which also corresponds to the temperature jump of cross-section 4 in Fig. 10(b). It is the formation of this secondary hot spot that leads to the failure of the device (Fig. 9), which plays a similar role to the hot spot near the contact pad in forward polarity.

As in the case of forward polarity, the increased resistance is mainly due to the temperature dependent resistivity of Al [Fig. 12(a)]. The dependency of temperature on Joule heating for different areas is illustrated in Fig. 12(b). While the temperature on the line (void 4) exhibits a linear dependence on Joule heating, the initial (void 2) and the secondary
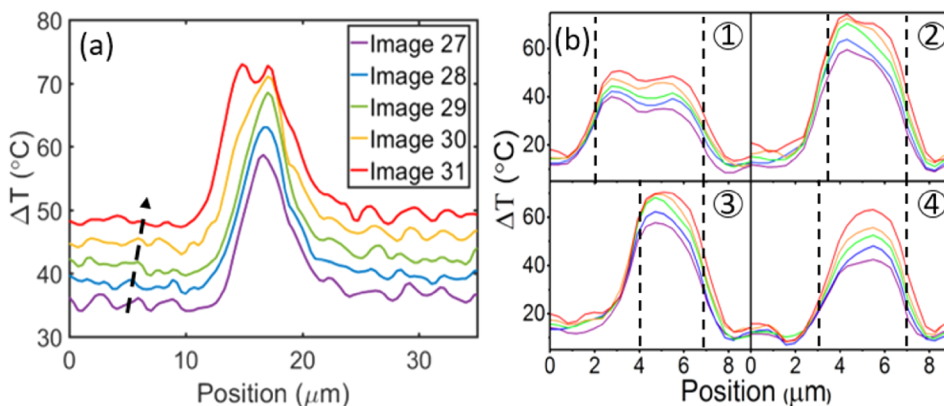

FIG. 10. (a) Change in temperature distribution along the black dashed line near void in Fig. 9(a). The black dashed arrow shows the trend of the increasing image number, corresponding to increasing time. (b) Temperature distribution along red dashed lines perpendicular to the test line as labeled in Fig. 9(a). Each subfigure is numbered following the definition in Fig. 9(a), and its legend is the same with (a). The black dashed lines indicate the boundary of the device.
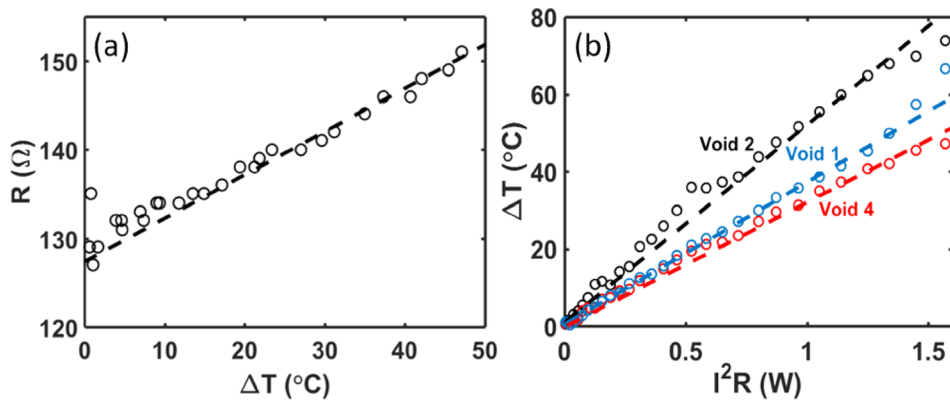
FIG. 12. (a) Increase in resistance with the temperature of box 4 of the void in Fig. 11. (b) Dependence of temperature on Joule heating power for box 1 (blue circle), box 2 (black circle), and box 4 (red circle) near the void in Fig. 11. The corresponding dashed lines in the figures are added for linearity guidance. The last two points of void 1 shows the temperature increasing beyond Joule heating due to EM induced structure degradation.

(void 1) hot spots show major temperature deviations from Joule heating predictions toward the end of the testing; at this point, the secondary hot spot subsequently causes the breakdown of the device. This effect is again likely related to the structure deformation and the current reconfiguration caused by electromigration, which warrants further investigation.

IV. DISCUSSION

A. Current density distribution when t = 0

In a wire with a variable cross-sectional area, regions with higher current densities require much more attention, considering that the electron wind, one of the most dominant factors in electromigration, is greatly enhanced. As shown in Fig. 13, two spots [e.g., junction between the pad and the wire and the void structure are shown in the Figs. 13(a) and 13(b), respectively] exhibit higher current density than rest of the wire. Obviously, the current density shows the peak
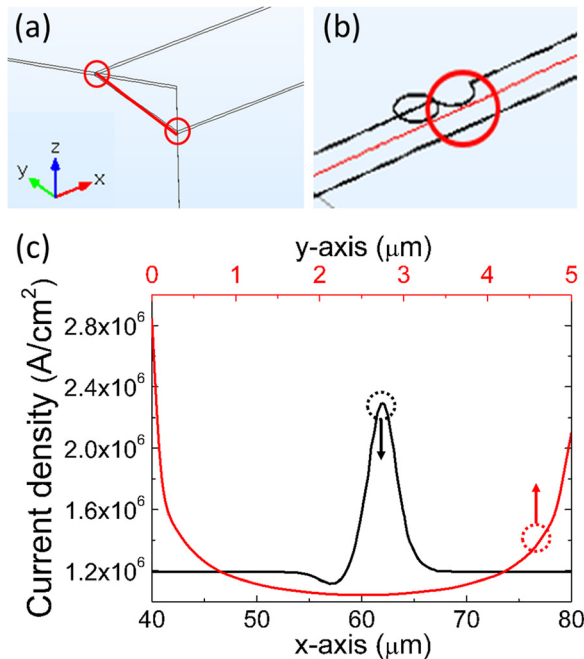

FIG. 13. Schematic of the simulated structure and circled regions show the spots where current density is high: (a) at the junction between the pad and the wire and (b) along the wire near the void. (c) Current density distribution along the red lines in (a) (red curve) and (b) (black curve).

value at the narrowest region along the current flowing direction [see the black line in Fig. 13(c)]. Interestingly, in the case of a thin metal wire, the current crowding causes a peak in the current density at the junction between the contact pad and the wire [see the red line in Fig. 13(c)]. The current crowding within the two narrowest locations will lead to hotspot formation, as demonstrated in the thermoreflectance measurements presented earlier. Since these two hot spots also experience the largest thermal gradients in the device, their overall susceptibility to electromigration is the greatest of anywhere along the length of the device. This analysis is of course consistent with the finding that failures consistently occur in these locations.

B. Sources of asymmetry

The analysis shown earlier, while pinpointing two likely locations of failure, does not predict which failures will occur first because of symmetry. However, an asymmetric reservoir-void structure provides differential failure modes, depending on the sign of the voltage. In the case of a long and thin wire, there are three key effects which can yield asymmetric failure locations depending on the polarity: (1) the electron wind effect from current flux (J_C), (2) the concentration gradient of atoms (J_D), and (3) the temperature gradient (J_T). For forward polarity, only the concentration gradient (J_D) effect can potentially be interpreted as consistent with the potential migration of atoms from the reservoir into the void where electron wind (J_C) and temperature gradient (J_T) effects induce atom depletion at the void. Considering that J_C and J_T have greater magnitudes than those of J_D, atomic depletion can form microvoids [see Fig. 4(b)]. At the same time, atoms are also leaving from the junction between the metal pad and the wire because of both electron wind (J_C) and temperature gradient (J_T) effects. In this work, for the forward polarity, the migration of atoms takes place more at the junction between a pad and a wire rather than at the reservoir, so that one can see the eventual failure position at the junction. However, the reverse polarity shows different failure positions. Countervailing forces associated with current, temperature, and atomic density gradients have different weightings, depending on the interconnect geometry.

Hot spots are found to play a crucial role in mediating the asymmetric response of current and temperature distributions to the geometry and as such have become a key

predictor of the failure of the device for both positive and negative polarities. For hot spots, both positive polarity at the contact pad and negative polarity near the void, the temperature just upstream of the electron wind is much lower than at the hot spot center [see Figs. 5(c) and 10(a)]. This is because the metal ions in hot spots can more easily move downstream with the electron current. However, an important distinction can be made, based on our data. For negative polarities, much cooler temperatures upstream manifest as a lack of upstream microvoids [e.g., see Fig. 9(b)]. It is different for the hot spot near the void at positive polarity since the temperature decreases more gradually upstream [see Fig. 5(b)]. Here, the metal ions are more energetic and move towards the void, which may help fill the depleted atom positions and prevent early failure. This is also consistent with upstream microvoid formation [see Fig. 4(b)]. Further simulation and experimental efforts are needed to fully quantify and optimize this hypothesized temperature gradient effect and to fully explain and predict likely asymmetric results in related structures.

V. CONCLUSION

To analyze electromigration failures, we proposed an asymmetric structure for electronic interconnects, consisting of a source and a reservoir of equal size. We characterized the surface temperature profile and the performance of this structure under increasing magnitude of voltage with both polarities under a total of four trials. We find that the failure mechanisms differ with the polarity of the voltage in a reproducible manner. For forward polarity, we find that Joule heating creates hot spots near the void and the contact pad. As the aluminum wires approach a critical current density of 21×10^6 A/cm^2, the temperature of the two hot spots increases significantly beyond the expected value of Joule heating. After less than an hour under these conditions, failure occurs at the contact pad, showing that self-healing may have filled the artificial void to prevent failure at that location. This is highly related to the electromigration-induced local structure deformation, which in turn changes the current distribution and accelerates the hotspot growth. In reverse polarity, similar hot spots form, but the temperature dependence on voltage differs from the prior case. Here, failure occurs just upwind of the induced void at a lower current density of 19×10^6 A/cm^2, showing that the reservoir cannot be used to affect electromigration in this configuration. In future work, it will be important to examine whether the distributed reservoir designs can suppress common failures in electronic interconnects and junctions.

ACKNOWLEDGMENTS

[1]J. R. Black, IEEE Trans. Electron Devices **16**, 338 (1969).
[2]F. M. d'Heurle, Proc. IEEE **59**, 1409 (1971).
[3]I. A. Blech and C. Herring, Appl. Phys. Lett. **29**, 131 (1976).
[4]J. Lienig, in *Proceedings of the 2006 International Symposium on Physical Design* (2006), pp. 39–46.
[5]I. A. Blech and E. Kinsbron, Thin Solid Films **25**, 327 (1975).
[6]A. Scorzoni, B. Neri, C. Caprile, and F. Fantini, Mater. Sci. Rep. **7**, 143 (1991).
[7]X. Chen, C. Liao, T. Wei, and S. Hu, IEEE Trans. Dependable Secure Comput. **9**, 770 (2012).
[8]I. H.-R. Jiang, H.-Y. Chang, and C.-L. Chang, in *Proceedings of the 19th International Symposium on Physical Design* (2010), pp. 177–184.
[9]G. Jerke and J. Lienig, IEEE Trans. Comput. Des. Integr. Circuits Syst. **23**, 80 (2004).
[10]J. Abella and X. Vera, ACM Comput. Surv. **42**, 9 (2010).
[11]B. F. Romanescu and D. J. Sorin, in *Proceedings of the 17th International Conference on Parallel Architectures and Compilation Techniques* (2008), pp. 43–51.
[12]J. Srinivasan, S. V. Adve, P. Bose, and J. A. Rivers, in *2004 International Conference on Dependable Systems and Networks* (2004), pp. 177–186.
[13]I. De Munari, A. Scorzoni, F. Tamarri, and F. Fantini, Semicond. Sci. Technol. **10**, 255 (1995).
[14]R. G. Filippi, G. A. Biery, and R. A. Wachnik, J. Appl. Phys. **78**, 3756 (1995).
[15]Y. Sun, P. Zhou, D.-Y. Kim, K. E. Goodson, and S. S. Wong, in *40th Annual Reliability Physics Symposium Proceedings* (2002), pp. 435–436.
[16]I. Ames, F. M. d'Heurle, and R. E. Horstmann, IBM J. Res. Dev. **14**, 461 (1970).
[17]D. Edelstein, J. Heidenreich, R. Goldblatt, W. Cote, C. Uzoh, N. Lustig, P. Roper, T. McDevitt, W. Motsiff, and A. Simon *et al.*, in *IEEE IEDM Technical Digest* (1997), pp. 773–776.
[18]H. V. Nguyen, C. Salm, R. Wenzel, A. J. Mouthaan, and F. G. Kuper, Microelectron. Reliab. **42**, 1421 (2002).
[19]M. J. Dion, in *2000 IEEE International Proceedings of the 38th Annual Reliability Physics Symposium* (2000), pp. 324–332.
[20]J. Lienig, in *Proceedings of the 2013 ACM International Symposium on Physical Design* (2013), pp. 33–40.
[21]T. Taychatanapat, K. I. Bolotin, F. Kuemmeth, and D. C. Ralph, Nano Lett. **7**, 652 (2007).
[22]W. Jeong, K. Kim, Y. Kim, W. Lee, and P. Reddy, Sci. Rep. **4**, 4975 (2014).
[23]J. C. Blair, P. B. Ghate, and C. T. Haywood, Appl. Phys. Lett. **17**, 281 (1970).
[24]I. A. Blech, J. Appl. Phys. **47**, 1203 (1976).
[25]O. Kraft, S. Bader, J. Sanchez, and E. Arzt, MRS Proc. **309**, 199 (1993).
[26]M. Farzaneh, K. Maize, D. Lüerßen, J. A. Summers, P. M. Mayer, P. E. Raad, K. P. Pipe, A. Shakouri, R. J. Ram, and J. A. Hudgings, J. Phys. D: Appl. Phys. **42**, 143001 (2009).
[27]T. Favaloro, A. Ziabari, J.-H. Bahk, P. Burke, H. Lu, J. Bowers, A. Gossard, Z. Bian, and A. Shakouri, J. Appl. Phys. **116**, 034501 (2014).
[28]K. Maize, J. Christofferson, and A. Shakouri, in *Twenty-Fourth Annual Semiconductor Thermal Measurement and Management Symposium (SEMI-THERM)* (IEEE, 2008), p. 55.
[29]K. Maize, A. Ziabari, W. D. French, P. Lindorfer, B. Oconnell, and A. Shakouri, IEEE Trans. Electron Devices **61**, 3047 (2014).
[30]R. E. Hummel, Int. Mater. Rev. **39**, 97 (1994).
[31]J. W. C. De Vries, Thin Solid Films **167**, 25 (1988).
[32]O. Kraft and E. Arzt, Acta Mater. **45**, 1599 (1997).
[33]H. Ceric and S. Selberherr, Mater. Sci. Eng., R **71**, 53 (2011).
[34]L. Cao, K. J. Ganesh, L. Zhang, O. Aubel, C. Hennesthal, M. Hauschildt, P. J. Ferreira, and P. S. Ho, Appl. Phys. Lett. **102**, 131907 (2013).
[35]L. Zhang, J. P. Zhou, J. Im, P. S. Ho, O. Aubel, C. Hennesthal, and E. Zschech, in *2010 IEEE International Reliability Physics Symposium (IRPS)* (2010), pp. 581–585.
[36]K. T. Lee, J. A. Szpunar, A. Morawiec, D. B. Knorr, and K. P. Rodbell, Can. Metall. Q. **34**, 287 (1995).